Collapse of a granular raft: Transition from single particle falling to collective creasing

Benjamin C. Druecke* and Ranit Mukherjee

Department of Mechanical Engineering, University of Minnesota, Minneapolis, Minnesota 55455, USA

Xiang Cheng

Department of Chemical Engineering and Materials Science, University of Minnesota, Minneapolis, Minnesota 55455, USA

Sungyon Lee of

Department of Mechanical Engineering, University of Minnesota, Minnesota, Minnesota 55455, USA



(Received 14 January 2022; accepted 26 January 2023; published 22 February 2023)

A granular raft—a two-dimensional (2D) particle layer floating at a fluid-fluid interface—collapses when losing its stability under compression. Although granular rafts are frequently encountered in various natural and engineering settings, how a raft fails under compression is still an open question. Here, by combining experiments with theoretical modeling, we examine the failure modes of granular rafts without free periphery under quasistatic biaxial compression. Different from granular rafts with open periphery, granular rafts in our study remain stable under finite compressive stresses. More surprisingly, under large compression, granular rafts made of small particles sink gradually by expelling individual particles, whereas rafts of large particles collapse catastrophically by forming large-scale creases. The collective creasing is enhanced by the 2D particle density and is suppressed by the density difference of the two fluids. We develop a one-dimensional continuum model for the shape of the granular rafts and the concentration of particles along the fluid-fluid interface, which provides quantitative explanations of our experimental findings.

DOI: 10.1103/PhysRevFluids.8.024003

I. INTRODUCTION

Particles of different sizes can assemble into two-dimensional (2D) rafts on a fluid-fluid interface through capillary interactions. While small colloids and nanoparticles adsorbed on a fluid-fluid interface are frequently used to stabilize fluid interfaces such as those in Pickering emulsions and cocontinuous blends [1–5], particle rafts composed of large granular particles are commonly seen in open environments with examples including the assembly of mosquito eggs [6], shade balls for water conservation [7], and sand particles deployed to clean oil spills [8]. These granular rafts contain the same in-plane forces as their small particle counterparts, but the body force of particles is equally important as the particle size becomes comparable or even larger than the particle-fluid capillary length, $\ell_c = \sqrt{\gamma_{12}/g(\rho_p - \rho_1)}$, where γ_{12} is the interfacial tension between the two fluids, g the acceleration, ρ_p the density of the particles, and ρ_1 the density of the more dense fluid.

^{*}bdruecke@gmail.com

[†]sungyon@umn.edu

Nevertheless, although the assembly of weightless rafts of small particles has been extensively studied [9–11], our understanding of the dynamics of heavy granular rafts is still primitive.

Much of the work on granular rafts focuses on the possibility to form and keep afloat a raft of N particles of diameter d [12]. When two particles are introduced, the asymmetric deformation of the fluid-fluid interface by gravity yields the spontaneous attraction of the particles. Known as the Cheerio effect, this capillary attraction is the basic building block of a granular raft. As the number of particles increases, the combination of the surface tension force, $\gamma_{12}P_{\rm raft}$, and the hydrostatic pressure must support the weight of the raft, $\sim Ng(\rho_p-\rho_1)d^3$, where $P_{\rm raft}\sim \sqrt{Nd^2}$ is the perimeter of the raft. The raft catastrophically collapses as the weight overwhelms the restoring forces with increasing N or d [8,13]. In particular, the collapse occurs when the in-plane stress of the raft becomes compressive [13,14], as the vertical component of a tensile traction on the periphery of the stable raft helps balance its weight.

In this paper, we consider a new regime of granular rafts, where we eliminate the free periphery of stable rafts. Surface tension, although still present to support individual particles and induce the Cheerio effect, is not required to stabilize rafts at the periphery in this scenario. Instead, the induced hydrostatic pressure balances the weight of rafts, obviating the need for surface tension to pull up against the gravitational force. The resulting rafts can sustain finite in-plane compressive stresses and exhibit two drastically different failure modes under large compression. Particularly, our experiments show that granular rafts made of small particles sink discretely by expelling individual particles, whereas granular rafts made of large particles collapse collectively by forming large-scale creases of many particles. Such an observation is quite unexpected, as small particles are subject to a stronger effect of surface tension and therefore more likely to float based on the existing theories of particle rafts.

The paper is organized as follows. Section II includes the experimental observations with water and hexane, while Sec. III provides a simplified theoretical model to explain the counterintuitive observations. We bring the theoretical and experimental results together in Sec. IV and conclude the paper with the summary and future work in Sec. V.

II. EXPERIMENTAL OBSERVATIONS

A granular raft on a fluid-fluid interface is formed by partially filling a conical funnel with water of density $\rho_1 = 1000 \text{ kg/m}^3$ followed by hexane of $\rho_2 = 655 \text{ kg/m}^3$ [15,16]. While we use a glass funnel of fixed inner diameter D = 6.5 cm and wall angle $\alpha = 32^{\circ}$ [Fig. 1(a)], the qualitative results are insensitive to the specific funnel chosen. We then deposit glass particles (density $\rho_p = 2300-2500 \text{ kg/m}^3$) onto the fluid-fluid interface. The mean particle diameter d is systematically varied from $90-1700 \, \mu\text{m}$, while the particle-fluid capillary length ℓ_c for this set of experiments corresponds to $\ell_c \approx 1.7 \, \text{mm}$.

The self-assembly of particles at the interface is sufficiently slow that particles first form finite-sized rafts with free periphery in the process of covering the entire interface. Hence, to ensure the formation of stable granular rafts with large particles (i.e., $d > 500 \,\mu\text{m}$), we first deposit particles on the water-air interface that can support heavier rafts than the water/hexane pair due to the larger difference in fluid densities and interfacial tension [14]. Once the raft covers the whole interface, we subsequently add hexane to the top. As the free periphery of the raft has been eliminated, the raft remains stable during the addition of hexane. For small particles with $d < 500 \,\mu\text{m}$, hexane is first deposited on top of the water, and the particles are allowed to sediment through hexane and directly assemble on the water-hexane interface. Note that glass particles are observed to rest on the hexane-water interface with a contact angle of $\theta = 45^{\circ} \pm 3^{\circ}$ and on the air-water interface with $\theta = 53^{\circ} \pm 6^{\circ}$, respectively.

Finally, we quasistatically impose equibiaxial compression to the interface by slowly draining water from the bottom of the funnel at a fixed rate, Q = 50 mL/min, using a syringe pump. The process decreases the surface area of the interface and jams the particles into one big granular raft. Note that withdrawing liquid from a funnel has been previously used to compress granular

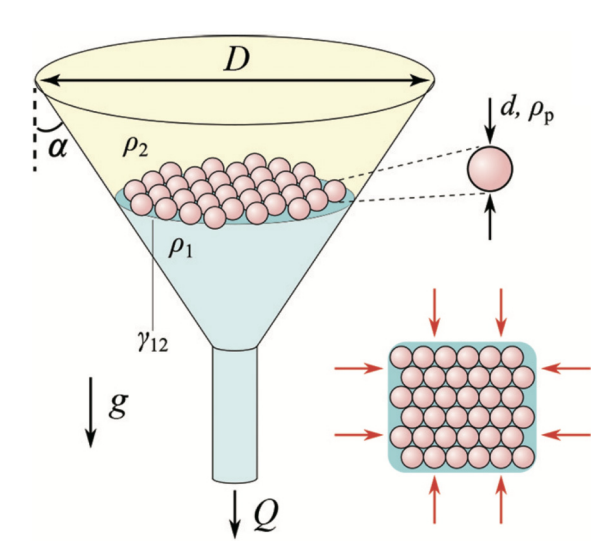


FIG. 1. A granular raft consisting of glass particles of diameter d and density ρ_p on a fluid-fluid interface is compressed equibiaxially as the lower fluid (density ρ_1) is drained from a conical funnel. The funnel wall makes angle α with the vertical axis, while D denotes the diameter of the widest part of the funnel.

aggregates [17] and an elastic ring [18] on a fluid-fluid interface. Owing to the geometry of the funnel, the drainage speed increases with the decreasing distance to the stem. However, we neglect the changes in the drainage speed in our analysis, as the failure mode of the raft is observed soon after we start draining. We also observe no qualitative changes in the experimental results when we vary Q from 10 mL/min to 88 mL/min.

In contrast to granular rafts with free periphery, the raft is stable under small compression. Then, as the compression is gradually increased, we observe that the raft fails in two distinct ways that depend on the particle diameter, as illustrated in the time-sequential images in Fig. 2. Movies illustrating the two different collapsing modes can also be found in the Supplemental Material [19]. First, for small particles (e.g., $d = 300-400\,\mu\text{m}$), the particles are expelled individually from the raft [Fig. 2(a)]. The side-view images in Fig. 2(a) show that the interface remains fairly flat except near the meniscus, as individual particles continuously fall out from the shrinking hexane-water interface. In addition, we do not observe significant changes in the particle distribution throughout the experiment, as the raft is shown to be well jammed in the top-down video [19]. However, additional experiments suggest that there are notable changes in the individual particle's vertical position prior to expulsion, a feature that will be further addressed in Sec. 3.

Second, for d = 1.0-1.3 mm, the raft collapses by forming system-wide creases with a large number of particles sinking collectively into water [Figs. 2(b)-2(c)]. This failure mode is similar to the collapse of granular rafts with free periphery under their own weights [8,13]. In contrast to the single particle falling regime, the side-view images of the experiment in Fig. 2(b) indicate that the raft starts to form large-scale deformations at early times (i.e., $t_0 = 6$ s). Then, as time progresses (i.e., $t_i - t_{ii}$), the crease near the funnel wall becomes dominant and eventually leads to the collapse of the whole raft at t_{iii} . The formation and growth of the crease near the funnel walls are more evident in the corresponding top-down images in Fig. 2(c), which also showcase the evolution in the particle distribution. In the top-down images, the granular raft appears to be fairly jammed, until the collapse at t_{iii} when the particles fall into the dominant crease and render the surrounding area less concentrated.

Finally, it is important to note that the granular raft does not remain flat near the funnel walls, as the hexane-water interface tends to curve down towards the funnel surface due to the difference in wettability between the two fluids. The meniscus shape ensures that there are more particles near

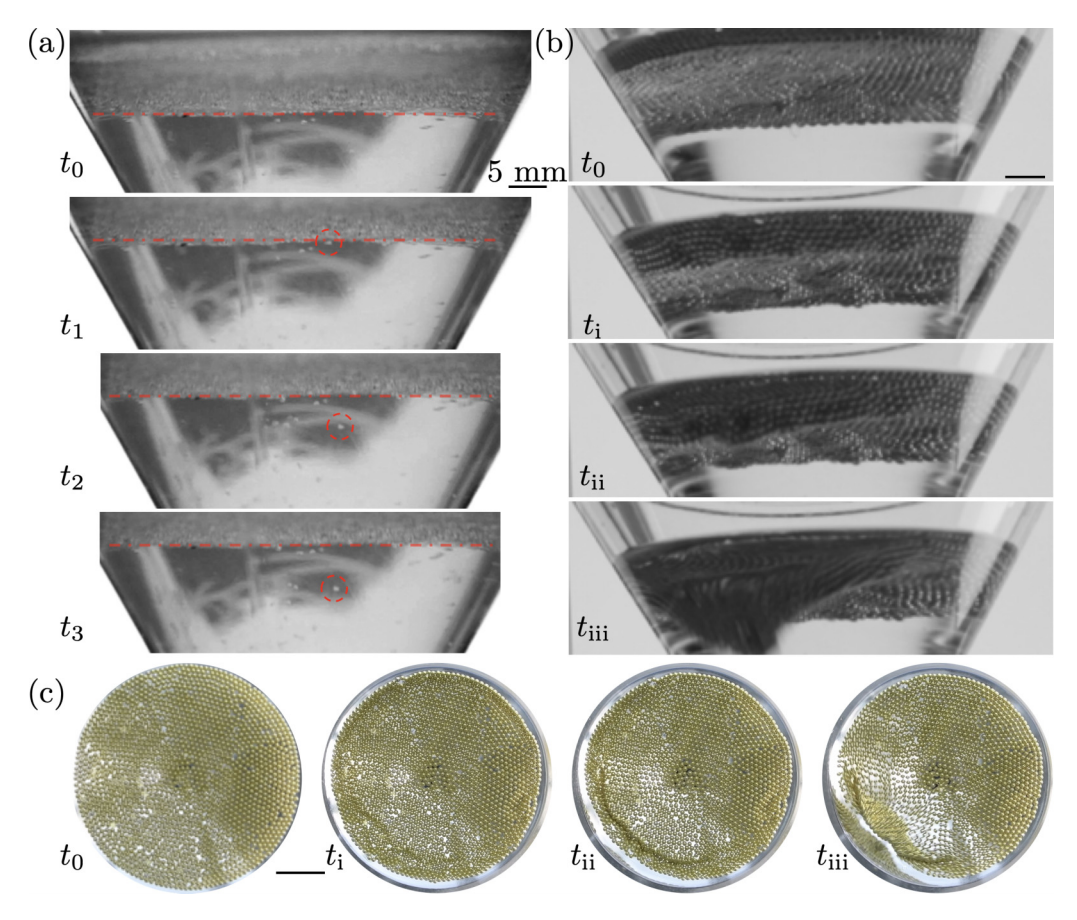


FIG. 2. (a) The time-sequential images of the granular raft with glass particles with $d=300-400\,\mu\mathrm{m}$ are observed to fall individually (highlighted by dashed circles) from the granular raft at an interface of water (bottom) and hexane (top), as water begins to be drained from below at time, $t_0=0$ s. Note that $t_1=0.08$ s, $t_1=0.6$ s, and $t_2=0.8$ s. (b) For the same liquids (water and hexane), the granular raft comprising glass particles (d=1.0-1.3 mm) collapses by collective creasing, where $t_0=6$ s, $t_i=7.4$ s, $t_{ii}=7.9$ s, and $t_{iii}=8.1$ s. (c) Top-down images at the same time stamps as (b) clearly show the formation of a crease near the funnel wall, which eventually collapses at t_{iii} . See also supplemental videos demonstrating the two failure modes.

the rim per projected area compared to the center of the raft. In turn, the enhanced weight of the raft near the rim partly influences the two failure modes. For instance, for rafts comprising large particles, creases leading to the raft's collapse tend to initiate more frequently near the meniscus, as illustrated in Fig. 2(c). However, creases can also form away from the meniscus, an example of which is included in Fig. 6 in Appendix A. For rafts that fail via single particle expulsion [Fig. 2(a)], particles fall out preferentially from the meniscus, instead of uniformly from the particle-laden interface (see the supplemental video [19]). While this may reduce the effects of compression on the center of the raft, some particles are still expelled from the center region as the bottom fluid is drained. Hence, we focus on the particle expulsion away from the funnel walls and neglect the effects of the meniscus in this paper.

III. THEORY

To rationalize the two modes of failure observed in the experiments, we consider a onedimensional model of the particle-laden interface under compression, which comes with a number of major simplifications. First, due to the 1D nature of our model, we cannot fully capture the dynamics of a 2D granular raft under biaxial compression. Second, we treat the raft as a continuum, which inherently neglects the discrete nature of the granular raft. As the current model cannot capture individual particles falling out of the raft, we hypothesize that the shape of the raft under compression is a prelude to the failure mode. Third, we assume that the particles are completely wetted by the lower fluid and do not exhibit interparticle frictional interactions for simplicity. Given these limitations, we do not aim to quantitatively reproduce the experimental results with our model. Instead, the purpose of our bare-bones theoretical model is to qualitatively capture the essential aspects of the observed phenomena and to uncover the physical mechanism behind the change of the failure mode of the granular raft.

A. 1D model of the jammed raft

We first consider the particle-laden interface with the vertical position, $\eta(s)$, defined as a function of arc length position, s, along the interface, as illustrated in Fig. 3(a). We assume the overall arc length of the raft is fixed and the number of particles per unit length ϕ is equal to the jammed concentration $\phi_J = 1/d$. The assumption yields a model analogous to that for a compressed elastic film proposed in Ref. [20] and later extended to account for the density difference of the two fluids [21]. Moreover, we assume there is no contact line pinning on the particles, so that the particles at the interface are free to rotate over its neighbors. This particle-level behavior results in no apparent bending modulus of the granular raft under compression [13,22]. Thus, we include no intrinsic bending energy in our continuum model.

Since the particles are everywhere jammed, the total surface area of the interface is fixed, with constant surface energy. The relevant energies are the gravitational potential energy of the two fluids,

$$U_{g,f} = \frac{1}{2} (\rho_1 - \rho_2) g \int_0^L \eta^2 \sqrt{1 - \left(\frac{d\eta}{ds}\right)^2} ds, \tag{1}$$

and the gravitational potential energy of the particles,

$$U_{g,p} = (\rho_p - \rho_1)g \frac{\pi d^2}{4} \int_0^L \eta \phi ds,$$
 (2)

where L is the length of the raft [21]. In addition, we constrain the liquid volume beneath the raft to $\eta_0 L$:

$$\Xi_V = \mathcal{R} \int_0^L \left[\eta \sqrt{1 - \left(\frac{d\eta}{ds}\right)^2} - \eta_0 \right] ds, \tag{3}$$

where η_0 is the height of the raft prior to compression, and \mathcal{R} is a Lagrange multiplier. This produces a hydrostatic pressure equal to the weight of the particles per unit projected area. We also impose the horizontal extent of the compressed raft to L_x with a Lagrange multiplier \mathcal{P} , such that

$$\Xi_{L_x} = \mathcal{P} \int_0^L \left[\sqrt{1 - \left(\frac{d\eta}{ds}\right)^2} - \frac{L_x}{L} \right] ds. \tag{4}$$

Then, putting the energies and constraints together, we obtain the following functional:

$$\Xi = \int_0^L \left[\left(\frac{\rho_1 - \rho_2}{2} g \eta^2 + \mathcal{P} + \mathcal{R} \eta \right) \sqrt{1 - \left(\frac{d\eta}{ds} \right)^2} + (\rho_p - \rho_1) g \frac{\pi d^2}{4} \eta \phi - \mathcal{P} \frac{L_x}{L} - \mathcal{R} \eta_0 \right] ds. \quad (5)$$

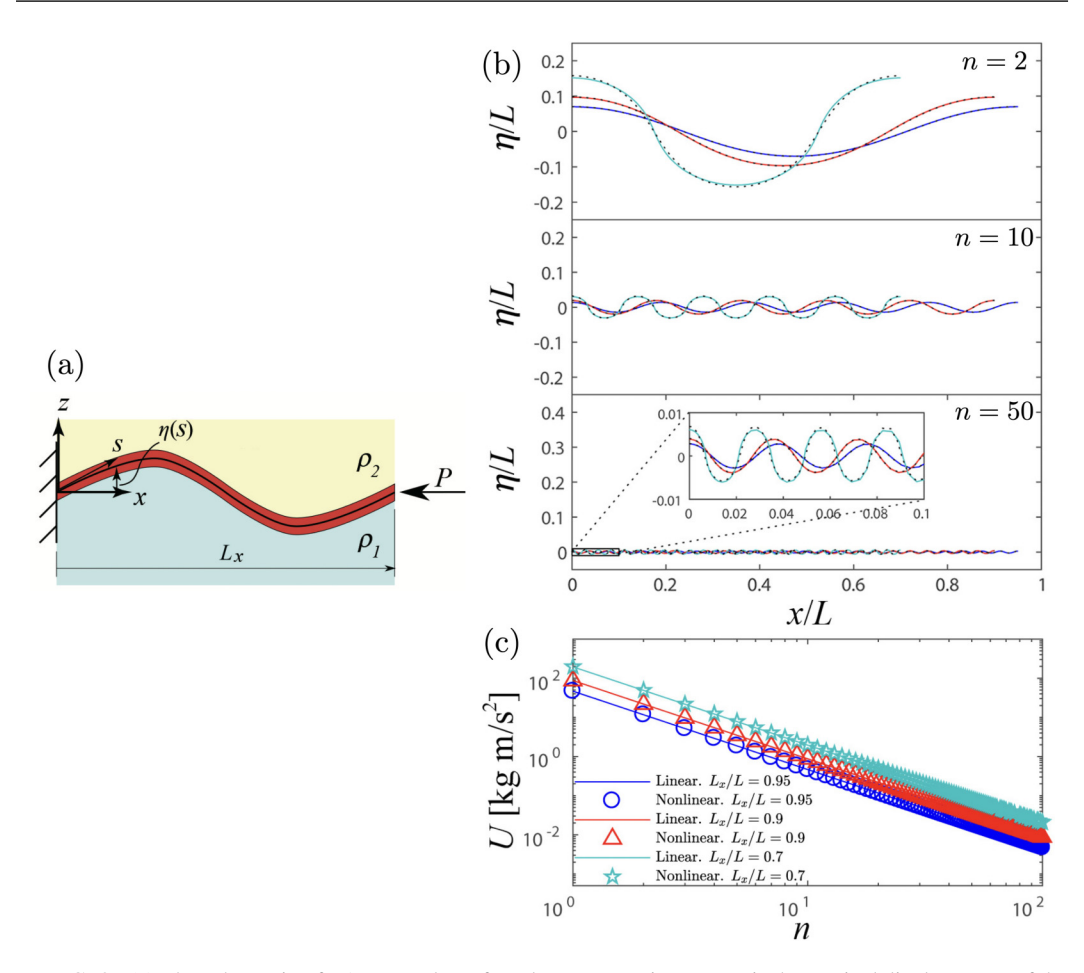


FIG. 3. (a) The schematic of a 1D granular raft under compression: $z = \eta$ is the vertical displacement of the raft, while s and x denote the arc length position and the horizontal coordinate, respectively; ϕ is the particle concentration along the raft. (b) The shape of the raft $\eta(x)$ for mode n=2 (top), 10 (middle), 50 (bottom), respectively, at varying levels of compression, L_x/L . $\rho_1 - \rho_2 = 1000 \, \text{kg/m}^3$, $\rho_p = 2500 \, \text{kg/m}^3$, $d=1 \, \text{mm}$, $g=9.81 \, \text{m/s}^2$, and $L=1 \, \text{m}$. The solid lines correspond to the analytical solutions in the limit of $d\eta/ds \ll 1$, while the dashed lines denote the full nonlinear solutions. (c) The total energy associated with the given raft shape is plotted as a function of n, which shows a monotonic decrease with increasing n.

To minimize the system energy, we take the first variation of $\Xi(\eta, \mathcal{P}, \mathcal{R})$ and use the integration by parts, to obtain the differential equation for $\eta(s)$:

$$\frac{d}{ds} \left[\left\{ \frac{(\rho_1 - \rho_2)g\eta^2 + \mathcal{P} + \mathcal{R}\eta}{2\sqrt{1 - \left(\frac{d\eta}{ds}\right)^2}} \right\} \frac{d\eta}{ds} \right] + ((\rho_1 - \rho_2)g\eta + \mathcal{R})\sqrt{1 - \left(\frac{d\eta}{ds}\right)^2} + (\rho_p - \rho_1)g\frac{\pi d^2}{4}\phi = 0, \tag{6}$$

in addition to the two constraints:

$$\int_0^L \eta \sqrt{1 - \left(\frac{d\eta}{ds}\right)^2} ds = \eta_0 L, \quad \int_0^L \sqrt{1 - \left(\frac{d\eta}{ds}\right)^2} ds = L_x. \tag{7}$$

Then, we linearize Eq. (6) in the limit of $d\eta/ds \ll 1$ to obtain

$$\mathcal{P}\frac{d^{2}\eta}{ds^{2}} + (\rho_{1} - \rho_{2})g\eta + \left[\mathcal{R} + (\rho_{p} - \rho_{1})\phi\frac{\pi d^{2}}{4}g\right] = 0,$$
(8)

which can be solved analytically, subject to $d\eta/ds = 0$ at s = [0, L].

We set $\mathcal{R} = -(\rho_p - \rho_1)g\phi\pi d^2/4$ via conservation of the fluid volume underneath the raft and $\eta_0 = 0$. Note that we can think of $-\mathcal{R}$ as the pressure that would be generated by setting a piston of weight per unit area $\rho_p g\phi V_p$ on the interface. With \mathcal{R} set, the problem becomes a homogeneous second-order differential equation with homogeneous boundary conditions, which gives rise to eigenvalues for the compressive force \mathcal{P}_n and sinusoidal interface shapes η_n , respectively:

$$\mathcal{P}_{n} = \frac{(\rho_{1} - \rho_{2})gL^{2}}{n^{2}\pi^{2}}, \quad \eta_{n} = C_{n}\cos(n\pi s/L).$$
 (9)

The linear solution is the superposition of these modes in some combination that satisfies the horizontal extent of the raft, or L_x . If we consider only a single mode at a time, we can compute C_n for the prescribed value of L_x/L , which is shown to decrease linearly with increasing n in Fig. 3(b). The full nonlinear solutions of η are also included (dashed lines) and closely match the linear solutions (solid lines) in Fig. 3(b). We compute the total energy associated with each n by plugging in η_n in Eqs. (1) and (2). As shown in Fig. 3(b), the total energy decreases quadratically with n, for both linear and nonlinear solutions. Note that $U_{g,p}$ does not affect the energy of the deformed raft, because the integral constraint for volume beneath the interface renders $U_{g,p}$ constant.

Hence, for a uniformly jammed raft, the model shows that the high wave-number modes are most energetically favorable. Indeed, for this continuum model with no bending and surface energies, the mode with infinite wave number would have zero amplitude and zero energetic penalty. In the physical system, infinite wave numbers are disallowed because the minimum wavelength must scale with the particle size. Instead, fixing the minimum wavelength as the particle diameter gives an interface shape in which alternating particles are displaced upward and downward, in a sawtooth configuration. Such a pattern is precisely the configuration observed in both experiments and models [23] before the expulsion of individual particles from the raft. In other words, this small-scale wrinkling is the precursor to individual particles leaving the interface. We include the experimental images that show the formation of particle-scale wrinkles prior to expulsion in the Appendix (see Fig. 7).

B. 1D model of the raft with variable ϕ

Overall, our simple model with constant ϕ successfully predicts single particle expulsion. However, the model lacks the dependence of the wrinkling mode on particle diameter, because the induced hydrostatic pressure perfectly offsets the weight of the particles. Furthermore, by fixing $\phi = \phi_J$, we ensure that there may only be instability in η , in addition to eliminating the effects of surface tension.

To address the experimental observations of size dependence and spatially varying ϕ , we construct a more general model with two dependent variables, η and ϕ . Distinct from the fixed ϕ model, both ϕ and η are set as functions of the horizontal coordinate x [see the schematic in Fig. 3(a)]. Hence, the potential energies of the fluids and the particles are given as the following:

$$U_{g,f} = \frac{1}{2}(\rho_1 - \rho_2)g \int_0^{L_x} \eta^2 dx, \quad U_{g,p} = (\rho_p - \rho_1)g \frac{\pi d^2}{4} \int_0^{L_x} \eta \phi \sqrt{1 + \left(\frac{d\eta}{dx}\right)^2} dx, \quad (10)$$

while constraining the volume of the lower liquid to V leads to $\Xi_V = \mathcal{R}[V - \int_0^{L_x} \eta dx]$ with the Lagrange multiplier, \mathcal{R} . Since the total length of the raft is no longer a fixed constant in this new model, we modify the second constraint to keep the number of particles on the raft to constant N,

such that

$$\Xi_N = \mathcal{Q} \left[N - \int_0^{L_x} \phi \sqrt{1 + \left(\frac{d\eta}{dx}\right)^2} dx \right],\tag{11}$$

where Q is the Lagrange multiplier.

In addition to the gravitational potential energies, $U_{g,f}$ and $U_{g,p}$, we include a soft interparticle repulsion energy

$$U_{pp} = \int_{0}^{L_{x}} \frac{kd^{2}}{2} \frac{(\phi - \phi_{J})^{2}}{\phi} H(\phi - \phi_{J}) \sqrt{1 + \left(\frac{d\eta}{dx}\right)^{2}} dx \tag{12}$$

and an interface energy between the two fluids

$$U_{12} = \int_{0}^{L_x} \gamma_{12} \frac{\phi_J - \phi}{\phi_J} H(\phi_J - \phi) \sqrt{1 + \left(\frac{d\eta}{dx}\right)^2} dx, \tag{13}$$

where $H(\cdot)$ is a Heaviside function, k the stiffness of the particle-particle repulsion, and γ_{12} the interfacial tension coefficient between the two fluids. Note that U_{12} becomes nonzero only in the regions with bare fluid-fluid interfaces (i.e., $\phi < \phi_J$), while U_{pp} is activated when $\phi > \phi_J$ to penalize the compression and resultant elastic deformation of the particles.

Similar to the 1D model with the fixed length, we derive the energy functional that we seek to minimize, by combining all the relevant energies and constraints: $\Xi(\phi, \eta, \mathcal{R}, \mathcal{Q}) = U_{g,f} + U_{g,p} + U_{pp} + U_{12} + \Xi_V + \Xi_N$. Then, we take the first variation of Ξ and include the effects of viscous energy dissipation to obtain a set of highly nonlinear differential equations for $\phi(x)$ and $\eta(x)$. The resultant equations are nondimensionalized based on $\eta^* = \eta/d$, $\phi^* = \phi/\phi_J$, $x^* = x/L_x$ with $L_x = 1$ m, the details of which are included in the Appendix. In addition to $\epsilon \equiv d/L_x$, the nondimensionalization yields the following key dimensionless parameters: $\mathcal{D}_1 \equiv (\rho_1 - \rho_2)/(\rho_p - \rho_1)$, $\mathcal{D}_2 \equiv d/\ell_c$, and $\mathcal{D}_3 \equiv d/\sqrt{kd/g(\rho_p - \rho_1)}$, where $\ell_c = \sqrt{\gamma_{12}/g(\rho_p - \rho_1)}$. As L_x and k are fixed in the simulations and not experimentally controlled, we primarily focus on the effects of systemically varying \mathcal{D}_1 and \mathcal{D}_2 . For given values of the dimensionless parameters, we solve the coupled PDE's for $\phi(x)$ and $\eta(x)$ numerically by using an overdamped transient with implicit time discretization, which is an iterative numerical method used to converge to stable equilibrium solutions. The interface displacement is initialized with a white noise profile. To preclude the flat interface solution, the particle concentration is initialized as a uniform concentration with slightly more particles than that needed to jam particles on a flat interface.

Representative results for interface shapes and particle distributions are shown in Fig. 4 for three different scenarios. In all three simulations, we fix $\rho_p = 2500 \text{ kg/m}^3$ (glass particles), $\rho_1 = 1000 \text{ kg/m}^3$ (water), $kd = 2 \times 10^5 \text{ N/m}$, and $\gamma_{12} = 72 \text{ mN/m}$. For $\mathcal{D}_1 \approx 0.67$ and $\mathcal{D}_2 \approx 0.45$ (i.e., d = 1000 µm, $\Delta \rho = \rho_1 - \rho_2 = 1000 \text{ kg/m}^3$), the simulation exhibits the low-energy mode of high wave-number wrinkling, consistent with the model with fixed ϕ discussed above (the red lines in Fig. 4). When \mathcal{D}_2 is increased to 0.68 (i.e., d = 1500 µm) with \mathcal{D}_1 fixed at 0.67 (i.e., $\Delta \rho = 1000 \text{ kg/m}^3$), the raft forms a sharp crease rather than uniformly distributed wrinkling. Notably, the raft becomes completely flat away from the crease, in clear contrast from the case with small-scale wrinkles. The sharp crease suggests the collapse of granular rafts via collective creasing for larger particles, which qualitatively matches the dependence of the failure mode on the particle size in the experiments.

In addition to the changes in d, we also consider the effects of modulating the density difference between the two fluids, or equivalently \mathcal{D}_1 , on the granular raft. When $\Delta \rho$ is decreased to 500 kg/m^3 while $d = 1000 \text{ }\mu\text{m}$ (i.e., $\mathcal{D}_1 \approx 0.33$, $\mathcal{D}_2 \approx 0.45$), the simulations in Fig. 4(a) reveal the formation of a sharp crease, indicative of the collective creasing mode. This suggests that the increase in d (i.e., \mathcal{D}_2) as well as the decrease in $\Delta \rho$ (i.e., \mathcal{D}_1) can both lead to the transition from individual particle

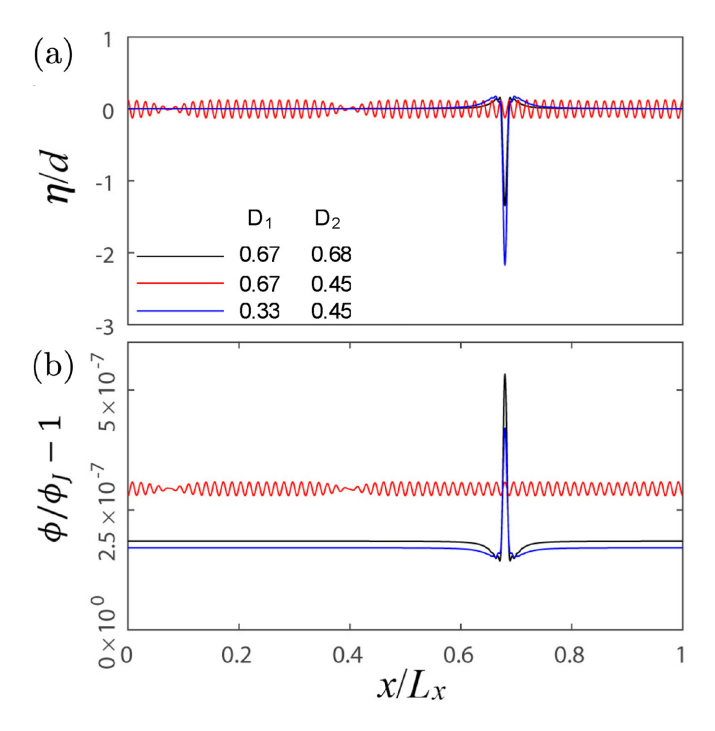


FIG. 4. (a) The computed shape of the raft $\eta(x)/d$ and (b) the corresponding particle concentration $(\phi(x)/\phi_J) - 1$: at different values of \mathcal{D}_1 and \mathcal{D}_2 . (Black line: $d = 1500 \,\mu\text{m}$, $\Delta \rho = 1000 \,\text{kg/m}^3$; red line: $d = 1000 \,\mu\text{m}$, $\Delta \rho = 1000 \,\text{kg/m}^3$; blue line: $d = 1000 \,\mu\text{m}$, $\Delta \rho = 500 \,\text{kg/m}^3$.)

expulsion to large-scale collective creasing. In addition, there is an evident coupling between the interface shape, η , and the particle concentration ϕ . Figure 4(b) shows the localization of high ϕ at the crease, which is consistent with the experimental observation of particles falling into the dominant crease. Hence, the results of our modified 1D model are able to qualitatively capture key aspects of the collective failure mode.

IV. TRANSITION IN FAILURE MODES

The results of our simple 1D model with variable ϕ have revealed the role of the particle diameter d and the density difference $\Delta \rho$ in causing the collapse of the raft by large-scale creases. Hence, we use this model to parametrically investigate the effect of d and $\Delta \rho$ for collective creasing, while $\rho_p = 2500 \text{ kg/m}^3$, $\rho_1 = 1000 \text{ kg/m}^3$, $kd = 2 \times 10^5 \text{ N/m}$, and $\gamma_{12} = 72 \text{ mN/m}$. We summarize the simulation results in the phase diagram of \mathcal{D}_1 versus \mathcal{D}_2 in Fig. 5. The phase diagram shows that the minimum value of \mathcal{D}_1 required for creasing increases linearly with \mathcal{D}_2 (Fig. 5), where collective creasing is denoted with an open circle, and particle-scale wrinkling with an open square. This suggests that for fixed ℓ_c , the minimum particle diameter above which creasing is observed increases linearly with $\Delta \rho$.

To experimentally verify the numerical results, we expand our experimental parameters to include different combinations of fluids beyond hexane and water (i.e., $\Delta \rho = 345 \text{ kg/m}^3$, $\mathcal{D}_1 = 0.23$), whose results are also included in Fig. 5 as filled symbols. For instance, granular rafts compressed on the air-water interface ($\Delta \rho = 999 \text{ kg/m}^3$, $\mathcal{D}_1 \approx 0.67$) are shown to exhibit single particle expulsion (blue square) for $\mathcal{D}_2 \lesssim 0.4$, or all particle diameters below d=1 mm, consistent with the numerical results. On the other hand, when \mathcal{D}_1 is decreased to 0.1 (i.e., water/mineral oil with $\Delta \rho = 135 \text{ kg/m}^3$), we experimentally observe collective creasing (red circle) for all values of

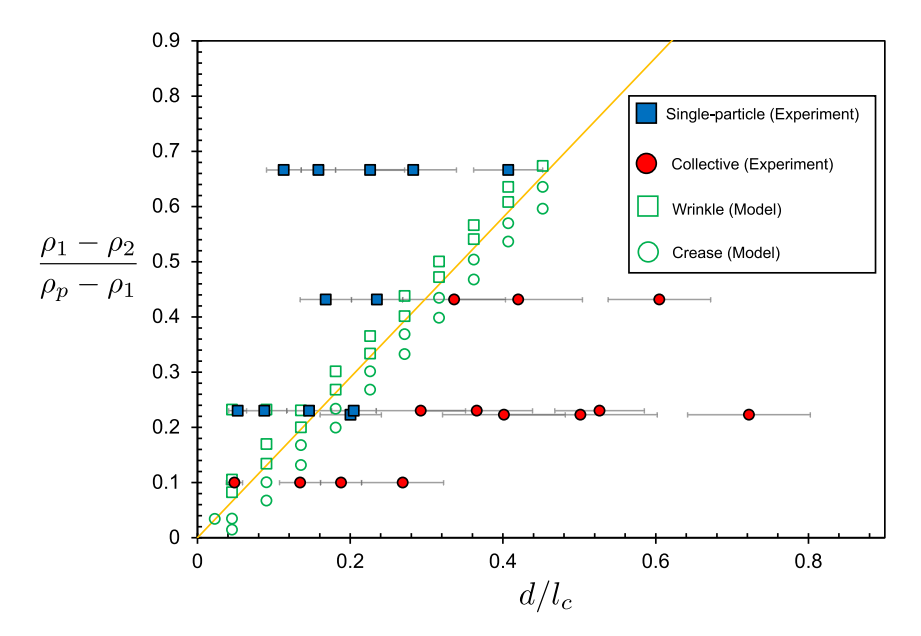


FIG. 5. The phase diagram illustrating the transition from wrinkling (single particle falling) to collective creasing with increasing $\mathcal{D}_2 = d/\ell_c$ and decreasing $\mathcal{D}_1 = (\rho_1 - \rho_2)/(\rho_p - \rho_1)$. Open symbols are from theory, whereas filled symbols are from experiments. The solid line indicates the phase boundary, while the horizontal error bars denote the size range of the particles used.

 d/ℓ_c , where $\ell_c \approx 1.86$ mm. This is in contrast to the simulation results that show the transition from creasing to wrinkling between $\mathcal{D}_2 = 0.045$ and $\mathcal{D}_2 = 0.090$. However, the experiment at $d = 90 \, \mu \text{m}$ (i.e., $\mathcal{D}_2 \approx 0.05$) is very close to the numerical transition point. Hence, given the inherent uncertainty in the particle size and experimental conditions, this mismatch between simulations and experiments does not represent a clear failure of the simplified 1D model.

The phase diagram also includes the experiments with fluid combinations that exhibit a clear transition in the failure mode with varying \mathcal{D}_2 . In particular, we conduct two sets of experiments with hexane on top and water on the bottom, one of which includes 5 wt% IPA in water with $\Delta \rho = 336 \text{ kg/m}^3$ (i.e., $\mathcal{D}_1 \approx 0.22$). For both cases, the failure mode of the granular raft is observed to transition from single particle falling to collective creasing as d is increased above 300 μ m. This transition corresponds to $\mathcal{D}_2 \approx 0.22$, which is slightly above the numerical transition from wrinkling (open green square) to creasing (open green circle) in Fig. 5. Similarly, experiments with the water-glycerol mixture as the lower fluid ($\Delta \rho = 556 \text{ kg/m}^3$, $\mathcal{D}_1 \approx 0.43$) exhibit collective creasing for $\mathcal{D}_2 \geqslant 0.34$, in remarkable agreement with the model results.

Both the experimental and numerical results presented in Fig. 5 clearly demonstrate the importance of $\Delta \rho$ and d in determining the failure mode of the granular raft. To rationalize this observation, we consider the fundamental balance for the creasing mode, which is the competition between the weight of the granular raft and the restoring force of buoyancy of the two fluids. We can think of this as akin to a Rayleigh-Taylor instability, where we have a medium-density lower fluid, a high-density particle layer and a low-density upper fluid. The weight of the granular raft per unit projected length corresponds to $\rho_p g d^2 \phi \sqrt{1 + (\partial \eta/\partial x)^2}$, while the restoring force from the liquids scales as $\Delta \rho g \eta$. When the weight of the raft per unit length overwhelms the restoring force of buoyancy (i.e., $\rho_p g d^2 \phi \sqrt{1 + (\partial \eta/\partial x)^2} > \Delta \rho g \eta$), the raft creases.

Based on this force balance, the necessary condition for collective creasing can be simplified to $\rho_p d > \Delta \rho \eta$ in the limit of $(\partial \eta/\partial x)^2 \ll 1$, as $\phi \sim 1/d$. This implies that when the interfacial deformation reaches the critical size of $\eta_c \sim \rho_p d/\Delta \rho$, the restoring buoyancy force becomes large

enough to stop the growth of the deformation and suppress creasing. However, if the interfacial slope also increases with η such that $(\partial \eta/\partial x)^2 \gg 1$, the destabilizing force now scales as $\rho_p g d |\partial \eta/\partial x|$, or $\rho_p g d (\eta/\lambda)$, where λ is the characteristic width of the deformation. Hence, in this limit, the creasing criterion becomes $\rho_p d (\eta/\lambda) > \Delta \rho \eta$, which suggests that the weight of the raft may overwhelm the restoring force, independent of η . These ideas together lead to the following condition for collective creasing: By the time η grows to $\eta_c \sim \rho_p d/\Delta \rho$, λ must be small enough to meet $(\eta/\lambda)^2 \gg 1$ and $\rho_p d/\lambda > \Delta \rho$, such that the interfacial deformation continues to grow, unimpeded. If we require $\eta_c/\lambda \gtrsim 1$, which simultaneously satisfies $\rho_p d/\lambda \gtrsim \Delta \rho$, the minimum particle diameter required for collective creasing corresponds to $d_c \sim \lambda(\Delta \rho/\rho_p)$.

Now, determining λ remains an open question. One possible choice for λ is the particle-fluid capillary length ℓ_c , such that $d_c \sim \sqrt{\gamma_{12}/g}(\rho_p-\rho_1)(\Delta\rho/\rho_p)$. This is consistent with the linear scaling between \mathcal{D}_1 and \mathcal{D}_2 observed in the numerical phase diagram. If we plug in the physical values into this scaling law, which reflects the experimental variations in γ_{12} and ρ_1 , we find that $d_c \approx [0.9, 0.3, 0.2, 0.1]$ mm for air-water ($\gamma_{12} = 72 \, \text{mN/m}$), hexane/glycerol ($\gamma_{12} = 28 \, \text{mN/m}$), hexane-water ($\gamma_{12} = 43 \, \text{mN/m}$), and mineral oil-water ($\gamma_{12} = 51 \, \text{mN/m}$), respectively. The resultant values of d_c are in qualitative agreement with the experimental findings summarized in Fig. 5. However, verifying this scaling law would require additional experiments, as the values of γ_{12} and ρ_1 have not been widely varied in the experiments. Furthermore, it is important to acknowledge that our current theoretical framework implicitly assumes the existence of a stable granular raft which requires the flotation of individual particles. Hence, we expect our simulations to become invalid as we lower γ_{12} or increase d and ρ_p in the experiments to the limit where individual particles are unstable at the interface. This limit will be considered in future studies.

Finally, it is noteworthy that the variation in ϕ is imperative to observe the creasing behavior, although it does not directly enter the scaling. While the onset of creasing does not require variation in ϕ , the particles need to be able to move preferentially towards the fold, for the instability to develop and for one dominant crease to emerge. This is further confirmed in Fig. 4(b), which shows a preferential increase in ϕ at the crease and a corresponding decrease in ϕ elsewhere, which acts to exacerbate the folding instability. When ϕ is not allowed to vary along the raft as in the fixed ϕ model, this transition to creasing is suppressed.

V. SUMMARY AND CONCLUSIONS

In this paper, we consider the dynamics of the granular raft by combining simple experiments and theory. We first form a raft of noncolloidal glass particles between two fluids inside a funnel and biaxially compress it to the point of failure by draining the lower fluid from below. Our systematic experiments reveal that the granular raft exhibits two distinct failure modes, depending on the particle diameter d and the density difference between the lower and upper fluids $\Delta \rho$. In particular, for small d and large $\Delta \rho$, individual particles are observed to fall out sporadically from the interface, as the raft is gradually compressed. By contrast, as d is increased or $\Delta \rho$ is lowered, the compressed raft tends to collapse by forming large-scale creases.

To rationalize the experimental observations, we construct a 1D continuum model of the raft based on the variational formulation. We compute the shape of the particle-laden interface that minimizes its total energy, building on a conjecture that the interfacial shape (i.e., small-scale wrinkles versus large-scale creases) corresponds to one of the two failure modes. The first iteration of the model with a uniformly jammed raft demonstrates that wrinkles with infinite wave number are most energetically favorable regardless of d and $\Delta \rho$, suggesting the single particle expulsion as the failure mode. We then relax the uniform ϕ constraint and numerically compute coupled η and ϕ . Remarkably, allowing the particles to move along the interface (or variable ϕ) is shown to be a sufficient condition for the collective creasing mode to emerge for large d and small $\Delta \rho$. We also develop a simple scaling law based on the competition between the weight of the granular raft and the restoring buoyancy force, which qualitatively matches both the numerical and

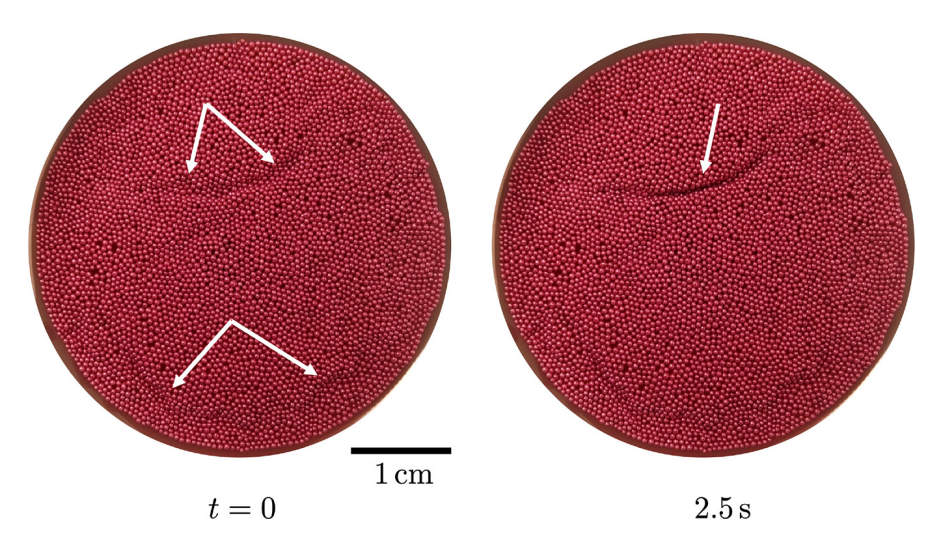


FIG. 6. The top-down images of the granular raft on a hexane-water surface comprising colored glass particles ($d = 625 \,\mu\text{m}$). The image on the left-hand side shows the formation of two creases at t = 0: one near the funnel walls (bottom) and one in the middle of the raft (top). At t = 2.5 s, the crease away from the walls appears to grow and leads to the collapse of the raft.

experimental observations. However, additional experiments are needed to further validate the scaling law.

From their formation to failure modes, the granular rafts explored in our study are purely driven by gravity, in stark contrast to colloidal rafts. The failure modes in the granular rafts are set by the weight of the particles in competition with the stabilizing buoyancy force, whereas the surface wettability of particles is shown to determine the behavior of the colloidal raft under compression [24]. Our model with no bending modulus qualitatively captures both failure modes, i.e., single particle falling and collective creasing, observed in our experiments. This modeling approach may be generalized to the colloidal limit by incorporating the energy associated with particle adsorption on the interface, to develop a unifying picture of particle rafts across length scales.

ACKNOWLEDGMENTS

This work was supported primarily by the National Science Foundation through the University of Minnesota MRSEC under Award No. DMR-2011401 and through CBET-2032354.

APPENDIX A: COLLECTIVE CREASING

While the top-down images in Fig. 2(c) show the formation of a large crease near the funnel walls, the creasing location is not limited to the meniscus. Figure 6 comprises the images of the granular raft with $d = 625 \,\mu\text{m}$ on a hexane-water surface. As the raft is compressed, we observe the creases form both near the meniscus (bottom) as well as near the center of the raft (top). Then, at $t = 2.5 \,\text{s}$, the crease near the center is shown to grow deeper, which leads to the collapse of the raft.

APPENDIX B: SINGLE PARTICLE EXPULSION

We hypothesize that small-scale wrinkles of our 1D model are a prelude to the expulsion of individual particles when the raft is compressed. While the particle-scale wrinkles may be too small to be visualized from the side-view images, the changes in the particle's vertical position can become

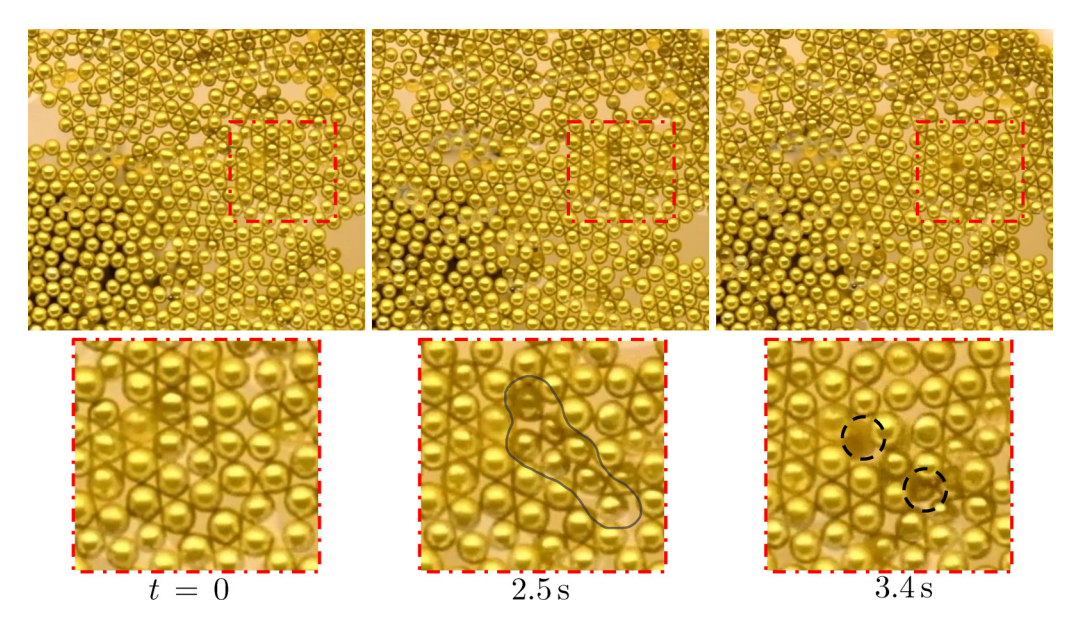


FIG. 7. The top-down image of the granular raft on an air-water surface comprising colored glass particles ($d \approx 1.0 \text{ mm}$). We focus on the evolution of the small region on the raft highlighted by an open square. The row of zoomed-in images on the bottom shows the formation of particle-scale wrinkles at t = 2.5 s. As the raft is further compressed at t = 3.4 s, two particles in particular are shown to grow darker, after which they are promptly expelled from the raft. Note that the pixel intensity is correlated with the vertical position of the particles.

evident from the top-down images if the particles are sufficiently large. Figure 7 shows a granular raft comprising colored glass particles ($d \approx 1.0$ mm) on an air-water interface. Specifically, the time-sequential images in Fig. 7 reveal the formation of a small wrinkle at t=2.5 s. As the raft is further compressed, the wrinkle becomes more localized and evolves into darkening of two particles (noted by dashed circles), after which the two particles promptly fall off the raft. This indicates that the particles are being lowered further into the funnel before they are expelled.

APPENDIX C: DERIVATION OF THE VARIABLE ϕ MODEL

We include the viscous dissipation into our variational formulation, so that the first variation of our total energy and constraints corresponds to

$$\delta U_{g,f} + \delta U_{g,p} + \delta U_{pp} + \delta U_{12} + \delta \Xi_V + \delta \Xi_N = \delta W_{\eta} + \delta W_{\phi}, \tag{C1}$$

where the work done by the viscous damping has contributions from the interfacial deformations (δW) and from the particle motion along the interface (δW_{ϕ}) :

$$\delta W_{\eta} = \int_{0}^{L_{x}} -c \frac{\partial \eta}{\partial t} \delta \eta dx, \quad \delta W_{\phi} = \int_{0}^{L_{x}} -c_{\phi} \frac{\partial \phi}{\partial t} \delta \phi dx.$$
 (C2)

Finally, by collecting terms that are linear in $\delta \eta$, $\delta \phi$, δQ , and $\delta \mathcal{R}$, respectively, we derive a set of coupled partial differential equations from Eq. (C1). We apply the periodic boundary for ϕ and $\partial \eta / \partial x = 0$ at $[0, L_x]$. The η profile is initialized with a white noise profile, while ϕ is set to be a uniform value that ensures that there are sufficient particles to jam the flat interface. Then, for given L_x , we numerically compute $\eta(x)$ and $\phi(x)$ by using backward Euler differentiation for its stability.

The resultant governing equations have been made dimensionless based on $\eta^* = \eta/d$, $\phi^* = \phi/\phi_J$, $x^* = x/L_x$, and $t^* = t/\tau$, where the asterisk denotes dimensionless variables. Here, τ is the characteristic time scale associated with interfacial deformations.

$$\mathcal{D}_{3}^{-2} \left[\frac{\phi^{*} - 1}{\phi^{*}} H(\phi^{*} - 1) \left(1 - \frac{\phi^{*} - 1}{2\phi^{*}} \right) + \frac{(\phi^{*} - 1)^{2}}{2\phi^{*}} \delta(\phi^{*} - 1) \right] - \mathcal{D}_{2}^{-2} [H(1 - \phi^{*}) + (1 - \phi^{*}) \delta(1 - \phi^{*})]$$

$$+ \frac{\pi}{4} \eta^{*} - \mathcal{Q}^{*} = -c_{\phi}^{*} \frac{\partial \phi^{*}}{\partial t^{*}} \left(1 + \epsilon^{2} \left(\frac{\partial \eta^{*}}{\partial x^{*}} \right)^{2} \right)^{-1/2},$$

$$-\epsilon^{2} \frac{\partial}{\partial x^{*}} \left[\frac{\partial \eta^{*}}{\partial x^{*}} \left(1 + \epsilon^{2} \left(\frac{\partial \eta^{*}}{\partial x^{*}} \right)^{2} \right)^{-1/2} \left\{ \frac{\mathcal{D}_{3}^{-2}}{2} \frac{(\phi^{*} - 1)^{2}}{\phi^{*}} H(\phi^{*} - 1) + \mathcal{D}_{2}^{-2} (1 - \phi^{*}) H(1 - \phi^{*}) - \mathcal{Q}^{*} \phi^{*} \right\} \right]$$

$$- \mathcal{R}^{*} + \frac{\pi}{4} \left[\phi^{*} \sqrt{1 + \epsilon^{2} \left(\frac{\partial \eta^{*}}{\partial x^{*}} \right)^{2}} - \epsilon^{2} \frac{\partial}{\partial x^{*}} \left\{ \eta^{*} \phi^{*} \frac{\partial \eta^{*}}{\partial x^{*}} \left(1 + \epsilon^{2} \left(\frac{\partial \eta^{*}}{\partial x^{*}} \right)^{2} \right)^{-1/2} \right\} \right] + \mathcal{D}_{1} \eta^{*} = -c^{*} \frac{\partial \eta^{*}}{\partial t^{*}},$$
(C4)

subject to the constraints: $V/(dL_x) = \int_0^1 \eta^* dx^*$ and $\epsilon N = \int_0^1 \phi^* \sqrt{1 + \epsilon^2 (\partial \eta^* / \partial x^*)^2} dx^*$. Note that $\delta(.)$ denotes the Dirac delta function. The complete list of dimensionless parameters in Eqs. (C3) and (C4) is as follows:

$$\mathcal{D}_1 \equiv \frac{\rho_1 - \rho_2}{\rho_p - \rho_1}, \quad \mathcal{D}_2 \equiv \frac{d}{\ell_c}, \quad \mathcal{D}_3 \equiv \frac{d}{\sqrt{kd/g(\rho_p - \rho_1)}}, \quad \epsilon \equiv \frac{d}{L_x}, \tag{C5}$$

$$Q^* \equiv \frac{Q}{(\rho_p - \rho_1)gd^3}, \quad \mathcal{R}^* \equiv \frac{\mathcal{R}}{(\rho_p - \rho_1)gd}, \quad c_\phi^* \equiv \frac{c_\phi}{(\rho_p - \rho_1)gd^4\tau}, \quad c^* \equiv \frac{c}{(\rho_p - \rho_1)g\tau}. \quad (C6)$$

^[1] W. Ramsden, Separation of solids in the surface-layers of solutions and 'suspensions' (observations on surface-membranes, bubbles, emulsions, and mechanical coagulation).—Preliminary account, Proc. R. Soc. Lond. 72, 156 (1904).

^[2] S. U. Pickering, CXCVI.-Emulsions, J. Chem. Soc., Trans. 91, 2001 (1907).

^[3] K. Stratford, R. Adhikari, I. Pagonabarraga, J.-C. Desplat, and M. E. Cates, Colloidal jamming at interfaces: A route to fluid-bicontinuous gels, Science 309, 2198 (2005).

^[4] L. Bai, J. W. Fruehwirth, X. Cheng, and C. W. Macosko, Dynamics and rheology of nonpolar bijels, Soft Matter 11, 5282 (2015).

^[5] L. Bai, S. He, J. W. Fruehwirth, A. Stein, C. W. Macosko, and X. Cheng, Localizing graphene at the interface of cocontinuous polymer blends: Morphology, rheology, and conductivity of cocontinuous conductive polymer composites, J. Rheol. 61, 575 (2017).

^[6] J. Loudet and B. Pouligny, How do mosquito eggs self-assemble on the water surface? Eur. Phys. J. E 34, 76 (2011).

^[7] E. Haghighi, K. Madani, and A. Hoekstra, The water footprint of water conservation using shade balls in california, Nature Sustain. 1, 358 (2018).

^[8] M. Abkarian, S. Protière, J. M. Aristoff, and H. A. Stone, Gravity-induced encapsulation of liquids by destabilization of granular rafts, Nature Commun. 4, 1895 (2013).

^[9] I. B. Liu, N. Sharifi-Mood, and K. J. Stebe, Capillary assembly of colloids: Interactions on planar and curved interfaces, Annu. Rev. Condens. Matter Phys. 9, 283 (2018).

^[10] J. C. Loudet, A. M. Alsayed, J. Zhang, and A. G. Yodh, Capillary Interactions Between Anisotropic Colloidal Particles, Phys. Rev. Lett. **94**, 018301 (2005).

^[11] P. Pieranski, Two-Dimensional Interfacial Colloidal Crystals, Phys. Rev. Lett. 45, 569 (1980).

^[12] D. Vella, Floating versus sinking, Annu. Rev. Fluid Mech. 47, 115 (2015).

- [13] S. Protière, C. Josserand, J. M. Aristoff, H. A. Stone, and M. Abkarian, Sinking a Granular Raft, Phys. Rev. Lett. 118, 108001 (2017).
- [14] D. Vella, P. D. Metcalfe, and R. J. Whittaker, Equilibrium conditions for the floating of multiple interfacial objects, J. Fluid Mech. 549, 215 (2006).
- [15] J. Van Hunsel and P. Joos, Stress-relaxation experiments at the oil/water interface, Colloids Surf. 25, 251 (1987).
- [16] B. L. Kim, A. Rendos, P. Ganesh, and K. A. Brown, Failure of particle-laden interfaces studied using the funnel method, Colloids Interface Sci. Commun. 28, 54 (2019).
- [17] M. Berhanu and A. Kudrolli, Heterogeneous Structure of Granular Aggregates with Capillary Interactions, Phys. Rev. Lett. 105, 098002 (2010).
- [18] A. L. Hazel and T. Mullin, On the buckling of elastic rings by external confinement, Philos. Trans. R. Soc. A 375, 20160227 (2017).
- [19] See Supplemental Material at http://link.aps.org/supplemental/10.1103/PhysRevFluids.8.024003 for the movies showing the two failure modes presented in Fig. 1, more details about the variational formulation, and a hypothetical model that demonstrates the transition.
- [20] H. Diamant and T. A. Witten, Compression Induced Folding of a Sheet: An Integrable System, Phys. Rev. Lett. 107, 164302 (2011).
- [21] E. Jambon-Puillet, D. Vella, and S. Protière, The compression of a heavy floating elastic film, Soft Matter 12, 9289 (2016).
- [22] C. Planchette, E. Lorenceau, and A. L. Biance, Surface wave on a particle raft, Soft Matter 8, 2444 (2012).
- [23] N. Fenwick, F. Bresme, and N. Quirke, Computer simulation of a langmuir trough experiment carried out on a nanoparticulate array, J. Chem. Phys. 114, 7274 (2001).
- [24] S. Razavi, K. D. Cao, B. Lin, K. Y. C. Lee, R. S. Tu, and I. Kretzschmar, Collapse of particle-laden interfaces under compression: Buckling vs particle expulsion, Langmuir 31, 7764 (2015).